

Braess's paradox and programmable behaviour in microfluidic networks

<https://doi.org/10.1038/s41586-019-1701-6>

Daniel J. Case¹, Yifan Liu², István Z. Kiss², Jean-Régis Angilella³ & Adilson E. Motter^{1,4*}

Received: 4 September 2018

Accepted: 1 August 2019

Published online: 23 October 2019

Microfluidic systems are now being designed with precision as miniaturized fluid manipulation devices that can execute increasingly complex tasks. However, their operation often requires numerous external control devices owing to the typically linear nature of microscale flows, which has hampered the development of integrated control mechanisms. Here we address this difficulty by designing microfluidic networks that exhibit a nonlinear relation between the applied pressure and the flow rate, which can be harnessed to switch the direction of internal flows solely by manipulating the input and/or output pressures. We show that these networks—implemented using rigid polymer channels carrying water—exhibit an experimentally supported fluid analogue of Braess's paradox, in which closing an intermediate channel results in a higher, rather than lower, total flow rate. The harnessed behaviour is scalable and can be used to implement flow routing with multiple switches. These findings have the potential to advance the development of built-in control mechanisms in microfluidic networks, thereby facilitating the creation of portable systems and enabling novel applications in areas ranging from wearable healthcare technologies to deployable space systems.

Fulfilment of the promise of microfluidics to operate as autonomous microscale networks in which fluids can be transported, mixed, reacted, separated and processed is no longer limited by experimental fabrication challenges, but rather by difficulties in creating built-in controls^{1–3}. The importance of this limitation can be appreciated by noting that the development of the modern microelectronics that form the basis of computer microprocessors was ultimately determined by the creation of integrated circuits, with all components fabricated on the same substrate. Microfluidics have already reached a level of integration in which networks with thousands of components, including control devices, are built on a single compact chip. However, in contrast with electronic integrated circuits, existing on-chip fluid control devices still need to be actuated externally. For example, microfluidic circuits fabricated from flexible polydimethylsiloxane (PDMS) can now incorporate a large number of control valves, which nevertheless have to be operated using control fluids through a control layer that lies on top of the working fluid network^{4,5}. As a result, microfluidics are still predominantly controlled by external hardware, despite substantial efforts over the past 20 years to develop systems with new control schemes^{6–10}. The construction of systems that forgo the current reliance on external hardware is crucial to further the development of portable microfluidic systems for pressing applications, ranging from point-of-care diagnostics and health monitoring wearables to analysis kits for field research^{11–14}. This requires developing next-generation integrated circuits in which not only the control devices but also the operation of those devices is integrated on-chip. The development of such a level of integration has been fundamentally limited by the fact that, at the microscale, fluid flows tend to respond linearly to pressure changes and thus cannot be easily amplified or switched.

In this Article, we explore new physics that emerges by combining network theory and fluid mechanics to induce nonlinear behaviour in microfluidics and effectively create a passive two-terminal flow-switch device that is entirely operated on-chip, directly by the working fluid. Previous work that has achieved built-in control capabilities (often externally actuated), including oscillatory flows^{15–18} and flow rate regulation^{19,20}, generally relied on flexible membranes and surfaces. Microfluidics with such flexible components require flows with very low Reynolds numbers—a regime in which fluid inertia, and thus the only nonlinear term of the Navier–Stokes equations for incompressible fluids, becomes negligible. This has led researchers to often discount the potential effects of fluid inertia on the flows (as reviewed, for example, in refs. ^{21,22}). Recent work has shown, however, that inertial forces can serve as a powerful on-chip tool to manipulate microfluidic dynamics locally^{23,24}, including shaping streamlines^{25,26}, mixing fluids²⁷ and directing particles^{28,29}. Here, we present networks designed to amplify inertial effects by incorporating properties of porous media that can be used for non-local fluid routing and manipulation of output patterns.

Figure 1a shows a schematic representation of a microfluidic system with the fundamental network structure we consider. It consists of five segments arranged as two parallel channels connected by a linking channel, where the inlets are kept at a common pressure P_{in} and the outlets are held at a common, lower, pressure, P_{out} . One of the outlet channels is modified to generate a nonlinear pressure–flow relationship, which is achieved by introducing an array of cylindrical obstacles. Our principal results are supported by theory, simulations and experiments, and they show that we can: (i) induce a flow direction switch through the linking channel solely by varying the pressure

¹Department of Physics and Astronomy, Northwestern University, Evanston, IL, USA. ²Department of Chemistry, Saint Louis University, St Louis, MO, USA. ³Normandie Université, UNICAEN, NIROUEN, ABTE, Caen, France. ⁴Northwestern Institute on Complex Systems, Northwestern University, Evanston, IL, USA. *e-mail: motter@northwestern.edu

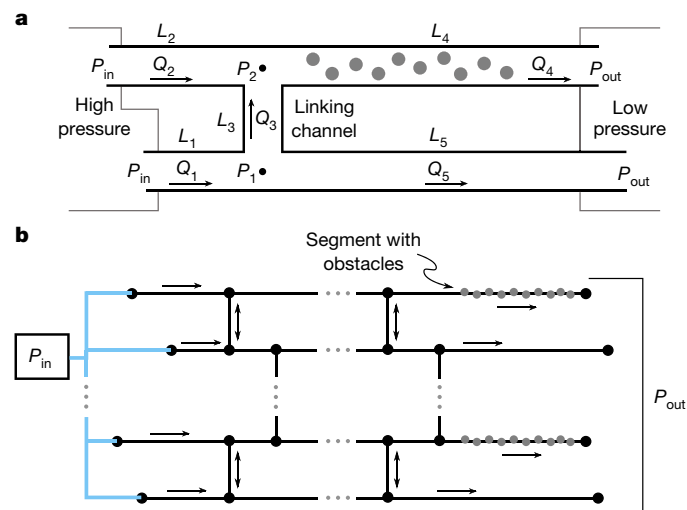


Fig. 1 | System schematics. **a**, Microfluidic network consisting of two parallel channels, joined by a linking channel, that connect high- and low-pressure fluid reservoirs. Grey filled circles represent stationary cylindrical obstacles. The labels denote pressures (P), channel lengths (L) and flow rates (Q), with arrows indicating the positive flow direction. **b**, Generic multiswitch microfluidic network consisting of an array of parallel channels interconnected by multiple linking channels. A subset of channel segments contain cylindrical obstacles. Flow is driven through the network by a single pressure difference ($P_{in} - P_{out}$).

difference between the inlets and outlets; and (ii) identify a pressure difference above which the total flow rate between the inlets and outlets increases on closing the linking channel. We also predict negative conductance transitions when the linking channel is equipped with an offset fluidic diode, which are transitions associated with non-monotonic pressure–flow relations analogous to those previously realized using flexible diaphragm valves³⁰. The counter-intuitive behaviour described in (ii) is formally equivalent to the so-called Braess’s paradox originally established for traffic networks^{31,32}, where closing a shortcut road has the possible effect of increasing net traffic flow. We demonstrate integration of the flow switch described in (i) by considering larger microfluidic networks, as illustrated in Fig. 1b, which incorporate multiple linking channels and are thus capable of exhibiting multiple flow switches. Flows through these networks are driven by a single pressure difference and yet can be designed to exhibit a variety of flow states by programming the pressure at which each flow switch occurs.

System design and nonlinearity

We consider conditions under which all channel segments have the same width w , the working fluid is water, and all surfaces (including obstacles) have no-slip boundaries. We assume, without loss of generality, that the pressure P_{out} at the outlets is zero, and consider scenarios in which either the static or the total pressure is controlled at the inlets (Methods). We examine two network configurations of the system in Fig. 1a: the connected configuration, in which the two parallel channels are allowed to exchange fluid through the linking channel; and the disconnected configuration, in which the linking channel is closed or removed. In our theoretical analysis and simulations, the flows are assumed to be two-dimensional, yet the main results carry over to three dimensions, as verified in our experiments.

For a straight microfluidic channel of length $L \gg w$ without obstacles, an approximate steady-state solution of the Navier–Stokes equations in two dimensions yields a linear relation between the total volumetric flow rate per unit depth Q and the pressure drop ΔP along the channel:

$$-\Delta P = \frac{12\mu L}{w^3} Q \quad (1)$$

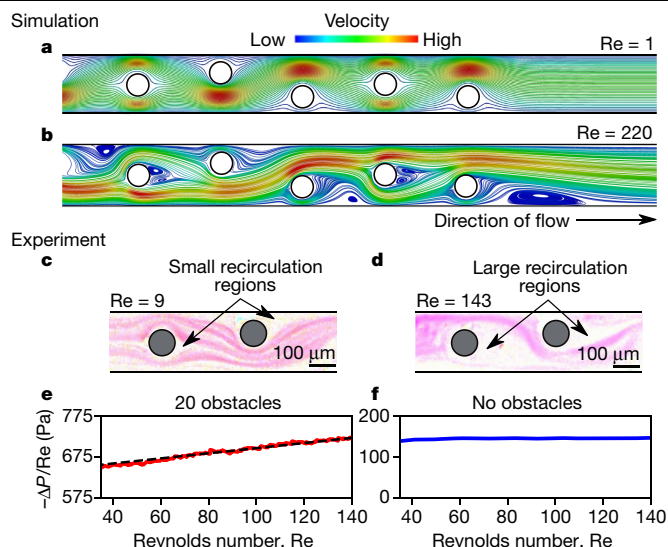


Fig. 2 | Development of nonlinear flow. **a, b**, Simulated flow in a channel with obstacles (open circles), showing no recirculation for low Re (**a**) and noticeable recirculation near the obstacles for larger Re (**b**). **c, d**, Experimentally observed flows around the obstacles (filled circles), visualized using pictures of fluorescent particles (marked in pink). The particle tracks trace the underlying flow structure, confirming the development of recirculation regions (white areas) as Re is increased from low (**c**) to moderate values (**d**). **e, f**, Experimentally measured relation between pressure loss and Re for a channel with (**e**; red curve) and without (**f**; blue curve) obstacles. The dashed line in **e** is a reference to guide the eye and indicates an approximately quadratic relation between pressure loss and flow rate.

where μ is the dynamic viscosity of the fluid. To induce deviations from this linear regime, we consider the effect of introducing multiple stationary obstacles in the channel. Figure 2a, b shows simulations of the Navier–Stokes equations for a channel with ten cylindrical obstacles of radius $r = w/5$ (Methods). We observe recirculation regions forming near the obstacles for sufficiently large Reynolds number $Re = 2\rho Q/\mu$, where ρ is the fluid density. The recirculation regions first appear for Re of the order of 10, and their number and size depend on Re . These localized structures are hallmarks of fluid inertia effects (and thereby of nonlinearity). We investigate how fluid inertia effects compound to impact the total flow rate by performing simulations across moderate values of Re when different numbers of obstacles are present. We find that a nonlinear relation between the pressure drop ΔP and flow rate $Q = \mu Re/2\rho$ emerges as soon as obstacles are introduced, and that the nonlinearity becomes more pronounced as the number of obstacles is increased (Supplementary Information section S3.1 and Supplementary Fig. 3).

The nonlinearity we observe in the relation between ΔP and Q conforms to the Forchheimer effect in porous media, which characterizes flow through many interconnected microchannels when local inertial effects at the points of interconnection are non-negligible, even for laminar flow^{33–35}. We use the Forchheimer equation to derive a relation between ΔP and Re for the channel with obstacles, given by

$$-\Delta P = \frac{\alpha\mu^2 L}{2\rho w} Re + \frac{\beta\mu^2 L}{4\rho w^2} Re^2 \quad (2)$$

where α is the reciprocal permeability and β is the non-Darcy flow coefficient, both depending solely on the system geometry (Methods).

The physical mechanism giving rise to this nonlinearity is the increase in flow recirculation and velocity gradients for larger Re , as evidenced in Fig. 2a, b for $Re = 1$ and 220. To test the impact of the inertial effects

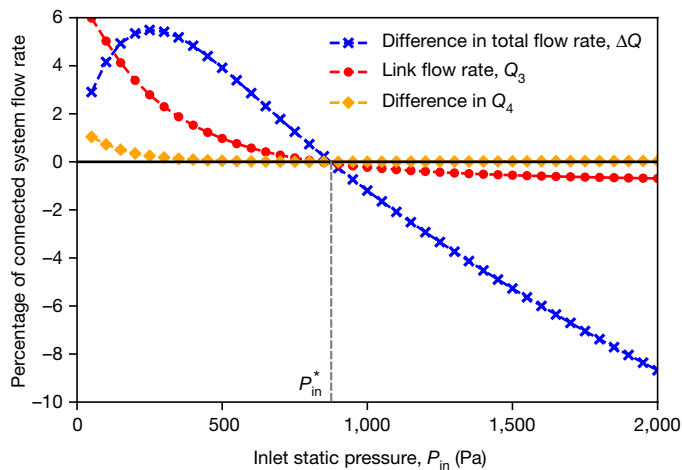


Fig. 3 | Braess's paradox and flow switching. Simulation results for the connected and disconnected configurations of the system for a range of inlet pressures P_{in} . The flow rates are presented as a percentage of the total flow rate through the connected system, Q_c , where we adopt the sign convention for the flow directions as defined in Fig. 1a. The flow through the linking channel switches direction at the critical pressure $P_{in} = P_{in}^*$, which coincides with the onset of negative ΔQ that marks the occurrence of Braess's paradox.

in realistic systems, we perform experiments using microchannels fabricated from stiff PDMS (hardened by curing). Figure 2c, d shows experimental evidence of the increase in the number and size of the recirculation regions with Re , in agreement with our simulations. An approximately linear relation between $-\Delta P/Re$ and Re (and thus an approximately quadratic relation between $-\Delta P$ and Q) for a channel containing 20 obstacles is shown in Fig. 2e, which contrasts with the constant relation measured for a channel without obstacles in Fig. 2f.

Switching and Braess's paradox

We incorporate the channel segment with obstacles characterized above into a network by considering the microfluidic system presented in Fig. 1a. We take the common static pressure P_{in} at the inlets to be the controlled variable in the system. The total flow rate through the network is now simply the sum of the flows at the outlets, $(Q_4 + Q_3)$. In Fig. 3, we present results for this system from direct simulations of the steady-state solutions of the Navier–Stokes equations. As P_{in} is increased from zero, the flow rate through the linking channel Q_3 is initially positive before changing direction and becoming negative once a critical pressure, defined as P_{in}^* , is reached (Fig. 3). This flow switch results from the nonlinear change in pressure loss along the channel segment containing obstacles, which causes a switch in the sign of the pressure difference along the linking channel ΔP_{21} (approximately $P_2 - P_1$) as the flow rate through the system increases with P_{in} . We define Q_c to be the total flow rate for the connected system configuration and Q_d to be the total flow rate for the disconnected system configuration, where both are regarded as functions of P_{in} .

Figure 3 shows $\Delta Q \equiv Q_c - Q_d$ for a range of applied pressures P_{in} . Intuition may suggest that ΔQ is positive for all values of P_{in} because the linking channel in the disconnected system can be considered to have an infinite fluidic resistance, while for the connected system configuration the resistance of the linking channel is finite. Hence, reducing the resistance of any component of the system may seem to imply that the total flow rate should increase for fixed P_{in} . We observe, however, that ΔQ becomes negative for P_{in} above the critical pressure that marks the flow switch, P_{in}^* , meaning that an open linking channel between the parallel channels results in a lower total flow rate. Figure 3 also shows that the flow rate through the channel segment with obstacles, Q_4 , remains largely unchanged between the two configurations. Therefore, the

difference in the total flow rate exists primarily in the difference in Q_5 , and Q_3 acts as a controlling variable of Q_5 .

The observation of a lower total flow rate for the connected configuration compared to the disconnected configuration for fixed P_{in} is a manifestation of a fluid analogue of Braess's paradox. Indeed, if we consider the disconnected system driven by an inlet pressure $P_{in} > P_{in}^*$, the addition of the linking channel can result in a decrease in the total steady-state flow rate (as large as 10% in our simulations). The value of the critical pressure P_{in}^* depends, of course, on the dimensions of the channels, but we find that the onset of Braess's paradox and the flow switch always occur at the same pressure for the range of parameters investigated. We obtain similar results for Braess's paradox and flow switching when instead the total pressure is controlled at the inlets (Supplementary Information section S3.4). Our observation of Braess's paradox and flow switching also has the potential to lead to additional control features when existing microfluidic components are integrated into our system. For example, by incorporating an offset fluidic diode³⁶ in the linking channel, the system can undergo negative (and positive) conductance transitions, where an increase in P_{in} leads to an abrupt decrease in the total flow rate (Supplementary Information section S4).

Experimental results

We performed experiments to validate our predictions of flow switching and Braess's paradox in a network with dimensions typical of microfluidics. A schematic of the experimental apparatus is presented in Fig. 4a, where an open/close valve is used to implement the addition/removal of the linking channel (Methods). With the valve open, a flow switch is observed at a critical driving pressure P_{in}^* in the range 5–10 kPa, as demonstrated in Fig. 4a by images of the flows through the channel junctions at the end points of this pressure range. (The switching behaviour has no reliance on the valve, as explicitly shown in Supplementary Fig. 11.)

A confirmation of Braess's paradox in this system is shown in Fig. 4b for driving pressures above P_{in}^* , as observed in our simulations. The measured total flow rate is higher when the linking channel valve is closed than when it is open, thus demonstrating the paradox, and the magnitude of the paradox is observed to be larger for higher driving pressures. A breakdown of how the flow rate changes in channel segments 4 and 5 individually is shown in Fig. 4c, d. Closing the valve causes the flow rates through both channels to increase, which is in agreement with direct simulations and is yet another striking aspect of Braess's paradox in this system; it would be, at first, intuitive to expect that Q_5 would decrease when the in-flow from the linking channel is switched off. Time series of the flow rates measured as the linking channel is sequentially opened and closed further illustrate the transitions underlying the paradox (as shown in Supplementary Fig. 12).

In our experiments, the total pressure is controlled at the inlets and the experimental results are in full qualitative agreement with simulations performed under the same pressure boundary conditions (Supplementary Information section S3.4). This illustrates the robustness of the phenomenon, given that our simulations are in two dimensions and three-dimensional effects are expected to be present in the experiments. We note that different aspects of the paradox have been considered in fluid networks, but only for macroscopic (that is, non-microfluidic) systems and while modelled by ad hoc flow equations^{37–39}. Analogues of the paradox have also been studied in several other areas, including electrical, mechanical, biological, and contemporary traffic networks^{40–44}. These examples show that Braess's paradox is a potentially general network phenomenon, which has remained unexplored in microfluidic networks.

Network model

To characterize the microfluidic system in Fig. 1a, we construct an analytic model that captures the flow properties observed in our simulations and experiments. The model consists of pressure–flow relations

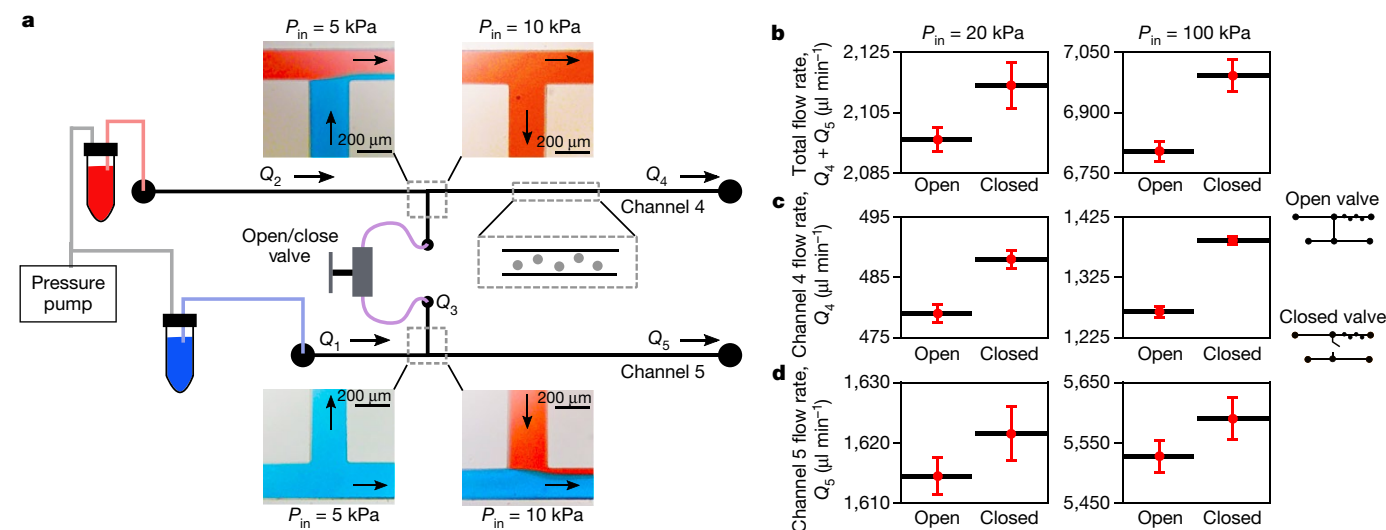


Fig. 4 | Experimental observation of flow switch and Braess's paradox. **a**, Experimental setup of the system presented in Fig. 1a, with flow tracking images (insets) at the junctions. An air-pressure pump is used to equally pressurize two vials containing red and blue dyed water, where each vial is connected to one of the system inlets. The linking channel is equipped with an open/close valve and channel 4 contains 20 obstacles. Images of the dyed flows through the junctions are shown for P_{in} below (5 kPa; left insets) and above (10 kPa;

right insets) the flow switching pressure P_{in}^* , where the flow directions are indicated by the arrows. **b**, Total flow rate ($Q_4 + Q_5$) when the linking channel valve is 'open' or 'closed' (see diagrams at right) for two different driving pressures above P_{in}^* . **c**, **d**, Breakdown of the total flow rate into Q_4 (**c**) and Q_5 (**d**) for the two states of the valve. The plotted flow rates are averages derived from time series data, and the error bars indicate one standard deviation. The observed increase in the total flow rate when the valve is closed is direct evidence of Braess's paradox.

for each channel segment and, crucially, includes the most dominant term resulting from minor pressure losses at the channel junctions^{45,46} (Methods). We model the contribution of the latter as an additive term $K(Q_3/Q_1)f(Q_3)$ to the pressure–flow equation for channel segment 5, where the scaling factor f and the coefficient K are increasing functions for $P_{in} \geq 0$ such that $f(0) = K(0) = 0$. Several results are obtained from this model for $P_{in} > 0$, as assumed throughout. First, if $\beta = 0$ (that is, the quadratic term is zero in equation (2)) when the static pressure is controlled or the dynamic pressure is negligible, then flow switching does not occur, in agreement with direct simulations (Supplementary Information section S3.2). Second, when $\beta > 0$, a steady-state solution can be found satisfying $Q_3 = 0$ provided that the following geometric condition is satisfied:

$$L_1 < \frac{12L_2L_5}{\alpha w^2L_4} = L^* \quad (3)$$

This solution identifies the critical pressure P_{in}^* . Third, for flow rates in the linking channel, the model predicts that a variation δQ_3 is negatively related to a variation δP_{in} around P_{in}^* . This indicates that P_{in} above (below) P_{in}^* results in a negative (positive) flow rate through the linking channel. The first result implies that, in our experiments, the Forchheimer effect is necessary to achieve a flow switch. The second and third results, which hold even for when dynamic pressure is non-negligible, show that this model captures the flow switching behaviour observed in the simulations and experiments. Importantly, we validate the flow-switching condition in equation (3) by demonstrating quantitative agreement between the model and simulations both when the static pressure and when the total pressure is controlled (Supplementary Information section S3.2).

The model also predicts Braess's paradox as observed in our experiments and simulations. Specifically, under the condition that equation (3) is satisfied and dynamic pressure is small (or static pressure is controlled), the model predicts the paradox to occur for $\delta P_{in} > 0$ if and only if

$$K'(0)\beta f\left(\frac{a}{\beta}\right) > c \quad (4)$$

where a and c are positive parameters and prime denotes derivative. If total pressure is controlled and dynamic pressure terms are included, the paradox is also predicted for $\delta P_{in} > 0$ provided that a relation similar to equation (4) is satisfied (details for both cases are presented in Supplementary Information section S2). The dependence of condition (4) on β and $K'(0)$ underlines the crucial roles of nonlinearity and minor losses in giving rise to Braess's paradox in our experiments, and shows in particular that minor losses have to be sufficiently large. Indeed, if the effect of minor losses is neglected, a manifestation of Braess's paradox is still predicted to occur, but with much smaller magnitude and only for $\delta P_{in} < 0$, which is inconsistent with our simulations and experiments (Supplementary Information section S2.3).

The result in equation (4) also highlights a fundamental difference between microfluidic and electronic circuits, namely that minor losses (that is, energy losses associated with interactions between circuit components) do not have direct analogues in common electronics. Given the central role played by such losses in equation (4), we posit that this difference might be the reason why no equivalent of the Braess paradox effect we present has been observed in electrical networks, even though aspects of it have⁴⁰. We further investigated the impact of interactions between channel segments by varying the junction angles to show that the paradox can be further enhanced by manipulating the minor losses (Supplementary Information section S3.3).

Networks with multiple programmed switches

The system considered thus far can be generalized to create larger microfluidic networks with multiple flow switches—that is, networks with multiple disjoint channel segments in which the flow initially in one direction can be individually 'switched' to move in the opposite direction through the manipulation of one driving pressure alone. In our design, the linking channel plays the role of a switch (and can be referred to as such). Figure 1b shows the multiswitch generalization of the network in Fig. 1a, which incorporates multiple linking channels and a subset of channel segments with obstacles. We experimentally demonstrate an instance of a six-switch network that exhibits flow switching in all linking channels (as presented in Supplementary Information section

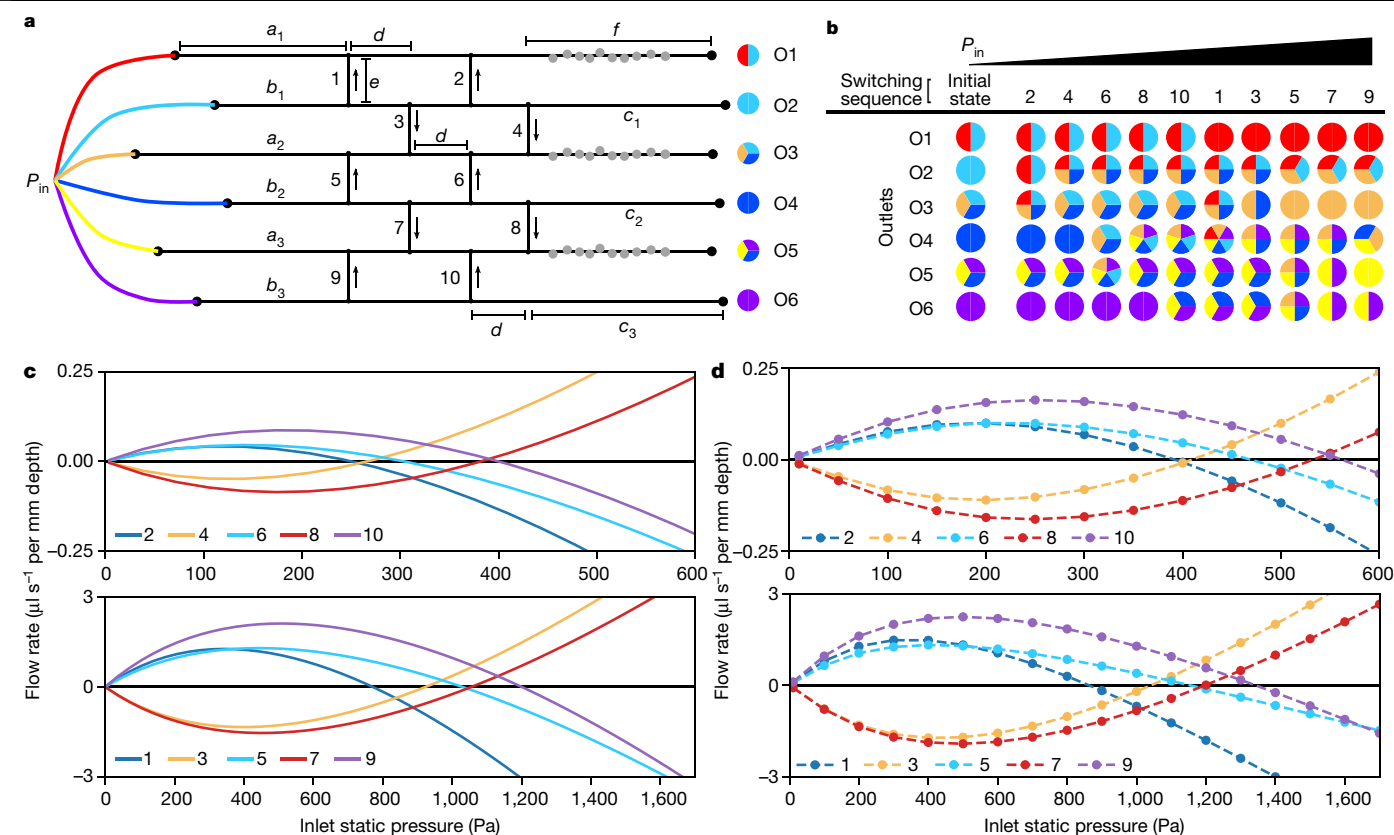


Fig. 5 | Flow patterns in a multiswitch network. **a**, Schematic of ten-switch network. Fluids of different colours are driven to each inlet by a common static pressure source, P_{in} . The outlets are labelled by O1–O6 and the linking channels by 1–10. The arrows indicate the flow direction through each linking channel and multicoloured circles schematically indicate the fluid composition at each outlet for an initially low P_{in} . The segment lengths are denoted by a_i , b_i , c_i , d , e and f , where a common length is assumed for all linking channels and the segments with obstacles are marked with filled grey circles. **b**, Patterns of outlet flows for the network programmed with a chosen switching sequence as P_{in} is increased. Each column of coloured circles denotes the outlet flows after the corresponding flow switch occurs, where mixing between different coloured

fluids is assumed to occur when passing through the same channel segment. **c, d**, Model predictions (**c**) and simulation results of the Navier–Stokes equations (**d**) for the flow rate through each linking channel for a network designed to exhibit the switching sequence in **b**. The flow rates are labelled according to the channels in **a** and are divided into two sets (top and bottom panels) for clarity. Positive flow rates correspond to flow in the upward direction in **a**, and each flow switch occurs when the corresponding curve crosses the horizontal axis. The segment dimensions that give rise to the particular switching order in **b–d** are reported in Supplementary Table 1. All 21 possible outlet flow colour combinations are realized between the switching sequence presented here and those in Supplementary Fig. 13.

S6.2). Multiswitch networks can be designed by extending the network model presented above.

One such network with ten linking channels is presented in Fig. 5a. By marking each inlet flow with a different colour, we show that a variety of patterns can form in the outlet flows (coloured circles in Fig. 5). The specific pattern at an outlet depends on the order in which the flow switches occur as P_{in} is varied. The network model for larger systems is constructed by combining pressure–flow relations for each channel segment with flow rate conservation equations for each junction. Using this model, we can design a network for which each flow switch occurs near a target value of P_{in} by optimizing the dimensions of the channel segments (Methods).

As illustrated in Fig. 5, a set of 11 different internal flow states and 17 unique colour combinations at the outlets are possible for the switching sequence realized in Fig. 5b. Figure 5c, d shows the agreement between the model predictions of these flow states and results from direct simulations of the Navier–Stokes equations. This variety of states (and output patterns) is achieved with only three channel segments containing obstacles and is parameterized by a single control variable—the driving pressure P_{in} . Moreover, the switching is implemented solely through the working fluid, which differs from existing approaches that rely on flexible valves and additional control flows¹⁵. Thus, multiswitch networks exhibit several properties exploitable in the design of new controllable microfluidic systems.

More generally, for a multiswitch network with n_c horizontal channels interconnected by n_l linking channels, the number of possible internal flow states is $n_l + 1$ if each linking channel exhibits a flow switch. In addition, the possible number of unique colour combinations in the outlet flows is $n_c(n_c + 1)/2$ if each inlet flow is marked with a different colour. All colour combinations can be realized over the set of all switching sequences, provided that there exist flow paths allowing mixing of every set of k adjacent colours for k ranging from 1 to n_c . The myriad states possible in such multiswitch networks underlie their ability to process inputs into multiple outputs and thus to support various applications, including implementing different mixing orders of chemical reagents and devising schemes for the parallel generation of mixtures with tunable concentrations.

Conclusions and outlook

The flow switch, conductance transitions and Braess’s paradox established in this study are all emergent behaviours of common origin resulting from nonlinearity and interactions between different parts of the system. The nonlinearity is directly determined by fluid inertia effects, which can be enhanced and manipulated through the placement of obstacles and has the advantage of not being reliant on flexible components, fluid compressibility or dedicated control flows. The onset of Braess’s paradox is marked by the flow-switching pressure, above which the increased resistance of the nonlinear channel causes the flow to be

routed in the negative direction through the linking channel. When constrained by a diode, the switch in flow direction also enables negative conductance transitions. Our results demonstrate an approach for routing and switching in microfluidic networks through control mechanisms that are coded into the network structure, thus responding to the call for design strategies that allow diverse microfluidic systems to be assembled from a small set of core components^{2,47}.

Here we considered the scenario in which the inlets and the outlets are (separately) held at the same pressure, rendering the network a two-terminal system in all cases, because this is the most stringent scenario for flow manipulation. If a multi-terminal system is configured, by allowing the pressures at each of the inlets (and/or outlets) to be varied independently, then the effects that we presented may be further enhanced. Finally, although we focused on boundary conditions in which the inlet pressures are controlled, it would be natural to explore in future research the scenario in which the controlled variables are the inlet flow rates. We anticipate, for example, that the negative conductance transitions would then be converted into pressure amplification (pressure release) transitions in which the inlet–outlet pressure difference increases (decreases) abruptly at the transition point. Accordingly, Braess’s paradox is also expected to take a complementary form in which closing the linking channel causes the inlet–outlet pressure difference to drop. Incidentally, it is this complementary form of Braess’s paradox that has been previously established for electrical circuits⁴⁰, thus suggesting an additional correspondence between electronic and microfluidic circuits.

Online content

Any methods, additional references, Nature Research reporting summaries, source data, extended data, supplementary information, acknowledgements, peer review information; details of author contributions and competing interests; and statements of data and code availability are available at <https://doi.org/10.1038/s41586-019-1701-6>.

- Pennathur, S. Flow control in microfluidics: are the workhorse flows adequate? *Lab Chip* **8**, 383–387 (2008).
- Stone, H. A. Microfluidics: tuned-in flow control. *Nat. Phys.* **5**, 178–179 (2009).
- Perdigones, F., Luque, A. & Quero, J. M. Correspondence between electronics and fluids in MEMS: designing microfluidic systems using electronics. *IEEE Ind. Electron. Mag.* **8**, 6–17 (2014).
- Thorsen, T., Maerkl, S. J. & Quake, S. R. Microfluidic large-scale integration. *Science* **298**, 580–584 (2002).
- Geertz, M., Shore, D. & Maerkl, S. J. Massively parallel measurements of molecular interaction kinetics on a microfluidic platform. *Proc. Natl Acad. Sci. USA* **109**, 16540–16545 (2012).
- Seker, E. et al. Nonlinear pressure-flow relationships for passive microfluidic valves. *Lab Chip* **9**, 2691–2697 (2009).
- Weaver, J. A., Melin, J., Stark, D., Quake, S. R. & Horowitz, M. A. Static control logic for microfluidic devices using pressure-gain valves. *Nat. Phys.* **6**, 218–223 (2010).
- Tanyeri, M., Ranka, M., Sittipolkul, N. & Schroeder, C. M. Microfluidic Wheatstone bridge for rapid sample analysis. *Lab Chip* **11**, 4181–4186 (2011).
- Kim, S.-J., Lai, D., Park, J. Y., Yokokawa, R. & Takayama, S. Microfluidic automation using elastomeric valves and droplets: reducing reliance on external controllers. *Small* **8**, 2925–2934 (2012).
- Li, L., Mo, J. & Li, Z. Nanofluidic diode for simple fluids without moving parts. *Phys. Rev. Lett.* **115**, 134503 (2015).
- Chin, C. D., Linder, V. & Sia, S. K. Commercialization of microfluidic point-of-care diagnostic devices. *Lab Chip* **12**, 2118–2134 (2012).
- Araci, I. E., Su, B., Quake, S. R. & Mandel, Y. An implantable microfluidic device for self-monitoring of intraocular pressure. *Nat. Med.* **20**, 1074–1078 (2014).
- Bhatia, S. N. & Ingber, D. E. Microfluidic organs-on-chips. *Nat. Biotechnol.* **32**, 760–772 (2014).
- Sackmann, E. K., Fulton, A. L. & Beebe, D. J. The present and future role of microfluidics in biomedical research. *Nature* **507**, 181–189 (2014).
- Leslie, D. C. et al. Frequency-specific flow control in microfluidic circuits with passive elastomeric features. *Nat. Phys.* **5**, 231–235 (2009).
- Mosadegh, B. et al. Integrated elastomeric components for autonomous regulation of sequential and oscillatory flow switching in microfluidic devices. *Nat. Phys.* **6**, 433–437 (2010).
- Duncan, P. N., Nguyen, T. V. & Hui, E. E. Pneumatic oscillator circuits for timing and control of integrated microfluidics. *Proc. Natl Acad. Sci. USA* **110**, 18104–18109 (2013).
- Duncan, P. N., Ahrar, S. & Hui, E. E. Scaling of pneumatic digital logic circuits. *Lab Chip* **15**, 1360–1365 (2015).
- Doh, I. & Cho, Y.-H. Passive flow-rate regulators using pressure-dependent autonomous deflection of parallel membrane valves. *Lab Chip* **9**, 2070–2075 (2009).
- Collino, R. R. et al. Flow switching in microfluidic networks using passive features and frequency tuning. *Lab Chip* **13**, 3668–3674 (2013).
- Stroock, A. D. et al. Chaotic mixer for microchannels. *Science* **295**, 647–651 (2002).
- Squires, T. M. & Quake, S. R. Microfluidics: fluid physics at the nanoliter scale. *Rev. Mod. Phys.* **77**, 977–1026 (2005).
- Amini, H., Lee, W. & Di Carlo, D. Inertial microfluidic physics. *Lab Chip* **14**, 2739–2761 (2014).
- Zhang, J. et al. Fundamentals and applications of inertial microfluidics: a review. *Lab Chip* **16**, 10–34 (2016).
- Tesaf, V. & Bandalusera, H. C. H. Bistable diverter valve in microfluidics. *Exp. Fluids* **50**, 1225–1233 (2011).
- Amini, H. et al. Engineering fluid flow using sequenced microstructures. *Nat. Commun.* **4**, 1826 (2013).
- Sudarsan, A. P. & Ugaz, V. M. Multivortex micromixing. *Proc. Natl Acad. Sci. USA* **103**, 7228–7233 (2006).
- Di Carlo, D., Edd, J. F., Humphry, K. J., Stone, H. A. & Toner, M. Particle segregation and dynamics in confined flows. *Phys. Rev. Lett.* **102**, 094503 (2009).
- Wang, X. & Papautsky, I. Size-based microfluidic multimodal microparticle sorter. *Lab Chip* **15**, 1350–1359 (2015).
- Xia, H. M. et al. Analyzing the transition pressure and viscosity limit of a hydroelastic microfluidic oscillator. *Appl. Phys. Lett.* **104**, 024101 (2014).
- Braess, D. Über ein Paradoxon aus der Verkehrsplanung. *Unternehmensforschung* **12**, 258–268 (1968).
- Braess, D., Nagurny, A. & Wakolbinger, T. On a paradox of traffic planning. *Transport. Sci.* **39**, 446–450 (2005).
- Rojas, S. & Koplik, J. Nonlinear flow in porous media. *Phys. Rev. E* **58**, 4776–4782 (1998).
- Andrade, J. S. Jr, Costa, U. M. S., Almeida, M. P., Makse, H. A. & Stanley, H. E. Inertial effects on fluid flow through disordered porous media. *Phys. Rev. Lett.* **82**, 5249–5252 (1999).
- Fourar, M., Radilla, G., Lenormand, R. & Moyne, C. On the non-linear behavior of a laminar single-phase flow through two and three-dimensional porous media. *Adv. Water Resour.* **27**, 669–677 (2004).
- Adams, M. L., Johnston, M. L., Scherer, A. & Quake, S. R. Polydimethylsiloxane based microfluidic diode. *J. Micromech. Microeng.* **15**, 1517–1521 (2005).
- Calvert, B. & Keady, G. Braess’s paradox and power-law nonlinearities in networks. *J. Aust. Math. Soc. Ser. B* **35**, 1–22 (1993).
- Penchina, C. M. Braess’s paradox and power-law nonlinearities in five-arc and six-arc two-terminal networks. *Open Transplant. J.* **3**, 8–14 (2009).
- Ayala, L. F. & Blumsack, S. The Braess paradox and its impact on natural-gas-network performance. *Oil Gas Facilities* **2**, 52–64 (2013).
- Cohen, J. E. & Horowitz, P. Paradoxical behavior of mechanical and electrical networks. *Nature* **352**, 699–701 (1991).
- Youn, H., Gastner, M. T. & Jeong, H. Price of anarchy in transportation networks: efficiency and optimality control. *Phys. Rev. Lett.* **101**, 128701 (2008).
- Nicolaou, Z. G. & Motter, A. E. Mechanical metamaterials with negative compressibility transitions. *Nat. Mater.* **11**, 608–613 (2012).
- Pala, M. G. et al. Transport inefficiency in branched-out mesoscopic networks: an analog of the Braess paradox. *Phys. Rev. Lett.* **108**, 076802 (2012).
- Motter, A. E. & Timme, M. Antagonistic phenomena in network dynamics. *Annu. Rev. Condens. Matter Phys.* **9**, 463–484 (2018).
- Crane Co. Engineering Division. *Flow of Fluids through Valves, Fittings, and Pipe*. Technical paper no. 410 (Crane Co., 2010).
- Khodaparast, S., Borhani, N. & Thome, J. R. Sudden expansions in circular microchannels: flow dynamics and pressure drop. *Microfluid. Nanofluidics* **17**, 561–572 (2014).
- Bhargava, K. C., Thompson, B. & Malmstadt, N. Discrete elements for 3D microfluidics. *Proc. Natl Acad. Sci. USA* **111**, 15013–15018 (2014).

Publisher’s note Springer Nature remains neutral with regard to jurisdictional claims in published maps and institutional affiliations.

© The Author(s), under exclusive licence to Springer Nature Limited 2019

Methods

Navier–Stokes simulations

The numerical simulations were performed using⁴⁸ OpenFOAM version 4.1. We used meshes with an average cell area ranging from $10\ \mu\text{m}^2$ to $340\ \mu\text{m}^2$, where the finest meshing was applied near the obstacles. All meshes were generated using Gmsh⁴⁹. The two-dimensional solutions were found using the simpleFoam solver within OpenFOAM, employing second-order numerical schemes, where a fixed static pressure of zero was set for the boundary conditions at the outlets. At the inlets, the static (total) pressure was fixed for the static (total) pressure controlled cases. For simulations of the multiswitch network in Fig. 5, the same geometry and dimensions were used as for the model predictions, provided in Supplementary Table 1, and equal driving pressures were applied at each of the six inlets.

Reynolds numbers

The characteristic length scale used in defining the Reynolds number of the flow is the hydraulic diameter of the channels, defined as $4A/P$, where A is the area and P is the perimeter of the channel cross-section (common to all segments). The hydraulic diameter in two and three dimensions is $2w$ and $2wh/(w+h)$, respectively, where h is the height of the channels in the three-dimensional case. The characteristic velocity used in two and three dimensions is Q/w and Q/wh , respectively. Therefore, we define $\text{Re} = 2\rho Q/\mu$ for our simulations in two dimensions and $\text{Re} = 2\rho Q/\mu(w+h)$ for our experiments in three dimensions. The undeclared ranges of Re for the channel segment with obstacles considered in the presented data are: 21–385 (Fig. 3), 12–121 (Fig. 4), 1–220 (Fig. 5), 1–380 (Supplementary Fig. 2), 4–111 (Supplementary Fig. 4), 40–385 (Supplementary Fig. 7), 20–400 (Supplementary Fig. 8), 2–10 (Supplementary Fig. 11b), 75–85 (Supplementary Fig. 11c), 76–89 (Supplementary Fig. 12), 10–20 (Supplementary Fig. 14b) and 110–120 (Supplementary Fig. 14c).

Pressure boundary conditions

We consider two different boundary conditions for the driving pressure P_{in} at the system inlets. Under one condition, total pressure is controlled and the inlets open directly into a high-pressure reservoir. Under the other condition, static pressure is controlled and the inlets are connected to the reservoir by pressure regulators. Total pressure is the sum of static pressure and dynamic pressure, where dynamic pressure is defined as $\frac{1}{2}\rho v^2$ for a fluid with density ρ and velocity v . The distinction between these boundary conditions is often neglected in the microfluidics literature when the Reynolds number is less than one⁵⁰, but it can become important for larger Reynolds numbers (even though the flow remains laminar)⁵¹.

Pressure–flow relations

We use equation (1) to describe the pressure–flow relation for straight, obstacle-free channels; it is derived directly from the Navier–Stokes equations by assuming plane Poiseuille flow through a two-dimensional channel. To describe the nonlinear pressure–flow relation observed for the channel with obstacles, we refer to the Forchheimer equation: $-\Delta P = \alpha\mu LV + \beta\rho LV^2$, where V is the average fluid velocity. In two dimensions, $V = Q/w = \mu\text{Re}/2\rho w$ and, thus, the Forchheimer equation can be written in the form of equation (2). In agreement with equation (2), we find an excellent linear fit between $-\Delta P/\text{Re}$ and Re for a channel with ten obstacles, and we validate the fit by predicting flows through the same channel for a fluid with a different viscosity (Supplementary Information section S3.1). We observe no unsteady flow through the channel with obstacles due to vortex shedding for Re of up to 400, as expected for systems with highly confined obstacles⁵², which permits the use of the steady-state relation in equation (2) over the range of Re considered here. We experimentally verify the source of nonlinearity in PDMS channels with obstacles, which were designed to have approximately square cross-sections to minimize deformation (which could lead to other forms of

nonlinearity^{53,54}). Through additional experiments, we confirmed that pressure–flow relations similar to those in Fig. 2e, f hold for channels constructed from materials with both higher rigidity (SU-8 photoresist) and lower rigidity (Flexdym) than the PDMS (Supplementary Information section S5 and Supplementary Fig. 10). We note that porous-like structures have been previously used both to study non-inertial effects in microfluidics, such as droplet formation⁵⁵ and viscous fingering⁵⁶, and to study inertial effects in larger systems⁵⁷. In our system, inertial effects arise at the microfluidic scale even for a much smaller number of obstacles than the typical number in porous-like materials.

Network flow model construction

The analytic model used to describe the system in Fig. 1a is constructed as follows: (i) we consider the pressure at the inlets P_{in} to be in the vicinity of P_{in}^* ; (ii) we approximate the pressure–flow relation through the linking channel as $Q_3 = \kappa(\gamma P_1 - P_2)$, where κ is the channel conductivity and γ is a free parameter allowing for an effective pressure difference; (iii) the flow equation for each other channel segment without obstacles is written as in equation (1), where $-\Delta P$ is the pressure drop along the segment and L is the segment length; (iv) for the channel segment with obstacles, we take the flow equation to be in the form of equation (2) (with Re expressed as $2\rho Q/\mu$); (v) we include the most dominant term resulting from minor pressure losses at the channel junctions. Therefore, the model consists of five pressure–flow relations, in addition to two flow conservation equations at the junctions: $Q_3 + Q_2 - Q_4 = 0$ and $Q_3 + Q_5 - Q_1 = 0$. When the static pressure is controlled at the inlets, the only nonlinearity that exists in the model comes from the Forchheimer term due to the presence of obstacles and the minor loss term. The model can also be adapted for when total pressure is controlled by taking the static pressure at each inlet to be $P_{\text{in}} - k\rho Q^2/2w^2$, where P_{in} now denotes total pressure and the coefficient k is a constant of order unity that only depends on the shape of the inlet velocity profile ($k \approx 1$ for a uniform velocity profile at the inlet, as considered here). However, the dynamic pressure term $\rho Q^2/2w^2$ is often negligible in real microfluidic systems because of the high pressures needed to drive fluid through the channels. Indeed, in our experiments, the dynamic pressure near P_{in}^* was smaller than the static pressure by two orders of magnitude and smaller than the pressure loss due to the Forchheimer effect by one order of magnitude. This can also be seen in Fig. 2f, where a constant relation between Re and $\Delta P/\text{Re}$ is measured. Details of the model are presented in Supplementary Information section S1.

Designing multiswitch networks

For a network with multiple switches and a given set of channel dimensions, the value of P_{in} for which a specific flow switch occurs can be determined through the addition of a constraint to the model that enforces the flow through the corresponding linking channel to be zero. Then, the dimensions of a chosen subset of channel segments may be varied through an optimization procedure in order to design a network for which each flow switch occurs near a target value of P_{in} . Depending on which dimensions are allowed to be adjusted, the desired relative order of the switches can be achieved exactly, and the final set of switching pressures can be very close to the target ones (often <5% difference), where the former is expected to be more important in applications. Further details on the design of multiswitch networks are presented in Supplementary Information section S6.1.

PDMS channel fabrication

The flow channels were assembled by sealing a patterned PDMS chip against a glass slide. The PDMS chip was made by pouring a mixture of PDMS oligomer and cross-linking curing agent (Sylgard 184) at a weight ratio of 10:1 into a mould after being degassed under vacuum. The mixture was cured at 74 °C for 1 h and then peeled off from the mould to yield the microchannel design. The dimensions of the channels in Figs. 2 and 4 were $200\ \mu\text{m}$ (width) \times $185\ \mu\text{m}$ (height), and the diameter of the obstacles was

97 μm . After punching the holes for inlet and outlet connections, the PDMS chip was thermally aged at 200 $^{\circ}\text{C}$ for 12 h to reduce pressure-induced deformation⁵⁸, yielding a chip with a Young's modulus of⁵⁹ approximately 3 MPa. Both the PDMS chip and the glass substrate were cleaned with isopropanol and treated by plasma for 90 s before bringing them into contact. Once the PDMS chip was sealed against the glass slide, the device was placed in an oven for 30 min at 74 $^{\circ}\text{C}$ to improve bonding quality.

The mould used was a silicon wafer containing microchannel patterns created by soft photolithography using a negative photoresist^{60,61}. A 4-inch silicon wafer (test grade, University Wafer, Boston, MA) was cleaned with acetone and isopropanol and dried with nitrogen gas. The wafer was then coated with SU-8 50 negative photoresist (MicroChem Corp., Newton, MA) on a spin coater (Laurell Technologies Corp., North Wales, PA) operating at 600 rpm for 30 s. After a pre-exposure bake at 65 $^{\circ}\text{C}$ and subsequently at 95 $^{\circ}\text{C}$, each for 60 min, the coated wafer was exposed to UV light (Autoflood 1000, Optical Associates, Milpitas, CA) through a negative transparent photomask that contained the desired channel design. Following a 3.5 min post-exposure bake at 95 $^{\circ}\text{C}$, the wafer was developed in SU-8 developer (MicroChem Corp., Newton, MA) for 60 min to obtain the pattern.

Flexdym channel fabrication

Flexdym (Blackholelab Inc., Paris) is a thermoplastic elastomer (Young's modulus of 1.18 MPa) with a rapid and easy moulding process for microfluidic devices⁶². After fabrication of the silicon wafer mould containing the channel designs, a sheet of Flexdym (6 cm \times 4 cm) was placed directly above the mould with another sheet of unpatterned PDMS (about 1 mm thick) placed above the Flexdym for protection. The whole set was then placed on a heat press between two Teflon sheets. The plate on the heat press was heated to 175 $^{\circ}\text{C}$ before starting to mould the Flexdym. Once the target temperature was reached, the lever on the heat plate was locked down with a timer set for 5 min. After the process was finished, the lever was released and the Flexdym sheet was inspected visually to make sure that no bubbles were trapped around the channel. The chip was allowed to cool down for 5 min before unfolding the layers. The Flexdym was permanently sealed with a glass slide by following the same sealing procedure used for the PDMS channels. The dimensions of the cross-section of the channels were 201 μm (width) \times 166 μm (height), and the diameter of the obstacles was 99 μm .

SU-8 photoresist channel fabrication

To make microfluidic channels directly from SU-8 photoresist, an inverse mask was designed and printed on transparency. The desired channel was printed on the inverse mask in black with transparent dots marking the obstacles, and the rest of the mask was left transparent. The same procedure used to make the silicon wafer master as described in Methods section 'PDMS channel fabrication' was followed to fabricate the channels on glass slides. The chip was then sealed by 3M VHB tape to another glass slide with holes for connections. The dimensions of the cross-section of the channels were 209 μm (width) \times 196 μm (height), and the diameter of the obstacles was 90 μm . The Young's modulus of SU-8 photoresist is 2 GPa (from the table of properties for SU-8 permanent photoresists, MicroChem Corp., Newton, MA, available at <http://microchem.com/pdf/SU-8-table-of-properties.pdf>).

Flow rate measurement

Experimental measurements in Figs. 2 and 4 were made with the system shown in Fig. 4a. When measuring the relation between pressure and flow rate, the linking channel valve was closed to allow separate measurement of the channel with and the channel without obstacles. Deionized (DI) water was pumped through each channel and a pressure scan from 0 to 100 kPa was performed using an Elveflow OB1 pressure controller. The flow rate was measured by an Elveflow MFS5 flow sensor (0.2–5 ml min^{-1}). To verify Braess's paradox, the same instruments were used and the pressure was set constant while recording the flow

rate at each outlet. Red (3 g l^{-1} , FD&C Red #40, Flavors & Colours) and blue (1.5 g l^{-1} , FD&C Blue #1, Flavors & Colours) dyes were added into DI water to demonstrate the switching behaviour. The concentrations of the dyes were adjusted for similar flow rate under the same pressure. The flow rate measurements in Supplementary Fig. 10 were performed using isolated channels constructed from Flexdym and SU-8 photore-sist, respectively.

Fluorescence imaging

Fluorescent polyethylene microspheres (10–20 μm) were suspended in Tween 80 solution (Cospheric LLC, Santa Barbara, CA) and pumped through a single microfluidic channel with obstacles by an Elveflow OB1 pressure controller. Two different pressures were applied, 3 kPa and 100 kPa, to demonstrate different flow profiles around the obstacles. Fluorescence images were captured with an Olympus BX51 microscope equipped with a NIBA filter through an Infinity 3 CCD camera.

Measured flow rate data and statistics

Savitsky–Golay filtering was applied to all flow rate data collected through experiments, using a window length of 11 data points and a second-order polynomial. For each of the fixed pressures presented in Fig. 4b–d, a 60 s time series of flow rate data was collected at each of the outlets with a sampling rate of 10 Hz. Over the 60 s interval, the linking channel valve was sequentially opened/closed every 15 s. For each time series, the 15 s intervals in which the valve was open (closed) were averaged to create a single 15 s time series for each outlet. The total flow rate ($Q_1 + Q_2$) was calculated when the valve is open and closed, respectively, by summing the 15 s time series for the two outlets point-by-point. The statistics presented in Fig. 4 are the average and standard deviation of the resulting series. For Supplementary Fig. 12, the flow rate at each of the two outlets was measured experimentally at a sampling rate of 100 Hz over a 180 s interval, during which the linking channel was sequentially opened/closed every 30 s. The total flow rate in Supplementary Fig. 12c was calculated by summing, point-by-point, the data in Supplementary Fig. 12a, b.

Parameters in simulations and experiments

In the simulations, we set $\rho = 10^3 \text{ kg m}^{-3}$, $\mu = 10^{-3} \text{ Pa s}$, $\nu = \mu/\rho = 10^{-6} \text{ m}^2 \text{ s}^{-1}$, $w = 500 \mu\text{m}$ for the width of all channels, and $r = 100 \mu\text{m}$ for the radius of all obstacles, unless otherwise noted. In all experiments, DI water was used as the working fluid. The other undeclared dimensions were as follows. In Fig. 2a, b, the length of the (partially shown) channel was 1.25 cm. In Fig. 2c–e, the channel length was 4.3 cm, and in Fig. 2f the channel length was 2.0 cm (see Methods section 'PDMS channel fabrication' for the remaining dimensions). In Fig. 3, $L_1 = 0.17 \text{ cm}$, $L_2 = 1.0 \text{ cm}$, $L_3 = 0.1 \text{ cm}$, $L_4 = 1.25 \text{ cm}$, and $L_5 = 1.0 \text{ cm}$. In Fig. 4, $L_1 = 0.6 \text{ cm}$, $L_2 = 2.9 \text{ cm}$, $L_4 = 1.4 \text{ cm}$ and $L_5 = 1.4 \text{ cm}$. For the linking channel, the switch valve was connected to the two parallel channels through 15 cm of round tubing and 0.7 cm of microchannel on each side. Each inlet was connected to the pressurized vials through 62 cm of tubing, and each outlet was attached to 50 cm of tubing. The inner diameter of all tubing was 0.79 mm.

Data availability

The datasets generated and/or analysed during the current study are available from the corresponding author on reasonable request.

Code availability

Custom Python code is available from the corresponding author on request.

48. OpenFOAM v4.1 (OpenFOAM Foundation, 2016).

49. Geuzaine, C. & Remacle, J.-F. Gmsh: a three-dimensional finite element mesh generator with built-in pre- and post-processing facilities. *Int. J. Numer. Methods Eng.* **79**, 1309–1331 (2009).

50. Oh, K. W., Lee, K., Ahn, B. & Furlani, E. P. Design of pressure-driven microfluidic networks using electric circuit analogy. *Lab Chip* **12**, 515–545 (2012).
51. Zeitoun, R. I., Langelier, S. M. & Gill, R. T. Implications of variable fluid resistance caused by start-up flow in microfluidic networks. *Microfluid. Nanofluidics* **16**, 473–482 (2014).
52. Zovatto, L. & Pedrizzetti, G. Flow about a circular cylinder between parallel walls. *J. Fluid Mech.* **440**, 1–25 (2001).
53. Gervais, T., El-ali, J., Gunther, A. & Jensen, K. F. Flow-induced deformation of shallow microfluidic channels. *Lab Chip* **6**, 500–507 (2006).
54. Christov, I. C., Cognet, V., Shidhore, T. C. & Stone, H. A. Flow rate–pressure drop relation for deformable shallow microfluidic channels. *J. Fluid Mech.* **841**, 267–286 (2018).
55. Amstad, E., Datta, S. S. & Weitz, D. A. The microfluidic post-array device: high throughput production of single emulsion drops. *Lab Chip* **14**, 705–709 (2014).
56. Haudin, F., Callewaert, M., De Malsche, W. & De Wit, A. Influence of nonideal mixing properties on viscous fingering in micropillar array columns. *Phys. Rev. Fluids* **1**, 074001 (2016).
57. Zhao, H., Liu, Z., Zhang, C., Guan, N. & Zhao, H. Pressure drop and friction factor of a rectangular channel with staggered mini pin fins of different shapes. *Exp. Therm. Fluid Sci.* **71**, 57–69 (2016).
58. Kim, M., Huang, Y., Choi, K. & Hidrovo, C. H. The improved resistance of PDMS to pressure-induced deformation and chemical solvent swelling for microfluidic devices. *Microelectron. Eng.* **124**, 66–75 (2014).
59. Johnston, I. D., McCluskey, D. K., Tan, C. K. L. & Tracey, M. C. Mechanical characterization of bulk sylgard 184 for microfluidics and microengineering. *J. Micromech. Microeng.* **24**, 035017 (2014).
60. Martin, R. S., Gawron, A. J., Lunte, S. M. & Henry, C. S. Dual-electrode electrochemical detection for poly(dimethylsiloxane)-fabricated capillary electrophoresis microchips. *Anal. Chem.* **72**, 3196–3202 (2000).
61. Duffy, D. C., McDonald, J. C., Schueller, O. J. A. & Whitesides, G. M. Rapid prototyping of microfluidic systems in poly(dimethylsiloxane). *Anal. Chem.* **70**, 4974–4984 (1998).
62. Lachaux, J. et al. Thermoplastic elastomer with advanced hydrophilization and bonding performances for rapid (30 s) and easy molding of microfluidic devices. *Lab Chip* **17**, 2581–2594 (2017).

Acknowledgements This research was supported by the US National Science Foundation (grants PHY-1001198 and CHE-1900011), the Simons Foundation (award number 342906) and a Northwestern University Presidential Fellowship.

Author contributions D.J.C., J.-R.A. and A.E.M. designed the overall study and formulated the theory. Y.L. and I.Z.K. designed and performed the experiments. D.J.C. implemented the numerical simulations and analyses. All authors contributed to the writing of the manuscript, which was led by D.J.C. and A.E.M. All authors reviewed and approved the final manuscript.

Competing interests The authors declare no competing interests.

Additional information

Supplementary information is available for this paper at <https://doi.org/10.1038/s41586-019-1701-6>.

Correspondence and requests for materials should be addressed to A.E.M.

Peer review information *Nature* thanks Sujit Datta and Dino Di Carlo for their contribution to the peer review of this work.

Reprints and permissions information is available at <http://www.nature.com/reprints>.